ChemPubSoc Europe

DOI: 10.1002/chem.201903158

CHEMISTRY
A European Journal
Communication

Electrode Materials

Integrated Bismuth Oxide Ultrathin Nanosheets/Carbon Foam Electrode for Highly Selective and Energy-Efficient Electrocatalytic Conversion of CO_2 to HCOOH

Fan-Lu Meng+,[a, b] Qi Zhang+,[a, c] Kai-Hua Liu,[a, b] and Xin-Bo Zhang*[a]

Abstract: Electroreduction of CO_2 into formic acid (HCOOH) is of particular interest as a hydrogen carrier and chemical feedstock. However, its conversion is limited by a high overpotential and low stability due to undesirable catalysts and electrode design. Herein, an integrated 3D bismuth oxide ultrathin nanosheets/carbon foam electrode is designed by a sponge effect and N-atom anchor for energy-efficient and selective electrocatalytic conversion of CO_2 to HCOOH for the first time. Benefitting from the unique 3D array foam architecture for highly efficient mass transfer, and optimized exposed active sites, as confirmed by density functional theory calculations, the integrated electrode achieves high electrocatalytic performance, including superior partial current density and faradaic efficiency (up to 94.1%) at a moderate overpotential as well as a high energy conversion efficiency of 60.3% and long-term durability.

Developing carbon-neutral economy and artificial CO_2 emissions fixation are imperative to solve energy and environmental issues.[1] Electrochemical conversion of CO_2 into high value added chemicals especially driven by renewable energy offers a promising strategy.[2] Despite rosy prospects, achieving this goal is full of challenges, including high kinetic barriers, and broad product distribution, mainly caused by the highly stable CO_2 molecule and complicated multielectron transfer.[3] To overcome these problems, a variety of electrocatalysts have been explored, including various metal candidates, carbon, complexes, and chalcogenides.[4,5] Wherein, precise control of crystallographic structure, composition and morphology,[6] oxide-derived strategy (e.g. reduced CuO_x, SnO_x, AuO_x)[7] and grain boundaries (GBs)[8] are devised to improve the activity and selectivity of CO_2 reduction.

HCOOH is a relatively high-value commodity chemical in various applications.[9] Currently, many sustainable replacements, such as hydrogenation of carbonate and bicarbonate,[10] hydrogenation,[11] electrochemical reduction, or photosynthetic production have been developed to convert CO_2 into HCOOH.[12] Electrochemical reduction presents the most promising strategy due to its controllability and existing mature electrolytic technologies and devices. Sn, Pd, and Bi are perhaps the most talked about catalysts for selectivity toward HCOOH.[9a–c] Of which, Bi is especially attractive because of its low toxicity and low cost and its ability to restrain the hydrogen evolution reaction. However, the performance of existing catalysts is limited by the bulk structure and unoptimized electrode design, in which the conventional inactive and non-conductive polymer binder would inevitably bury active sites, lead to random aggregation and limited mass transport. Alternatively, directly integrating nanostructured catalysts with current collectors to fabricate integrated electrodes is adopted as an efficient strategy.[13] Some reports have focused on modifying various metal foils into integrated electrodes, but, the low specific surface area, metallic substrate corrosion, and inhomogeneity limit the activity and stability. A foamlike conductive substrate with 3D skeleton structure will be the mostly attractive candidate, due to advantages of high aspect ratio structure, chemical stability, liquid absorbability with enough growth space, and open framework with high efficiency mass transfer.[14] Additionally, in view of different requests and standards within diversified reactors, prominent physical flexibility and mechanical strength would make a foam electrode more successful and meaningful. As far as we know, there is almost no report on constructing of 3D foam electrode for electrocatalytic CO_2 reduction, to say nothing of flexibility and high HCOOH selectivity and activity.

In response, as a proof-of-concept experiment, the strategy of integrating bismuth oxide ultrathin nanosheets on a flexible 3D carbon foam electrode and following electrochemical activation is proposed to solve the above difficulty for enhanced performance of electrocatalytic CO_2 reduction. Unexpectedly, the obtained integrated 3D foam electrode shows excellent

---

[a] F.-L. Meng,+ Q. Zhang,+ K.-H. Liu, Prof. Dr. X.-B. Zhang
State Key Laboratory of Rare Earth Resource Utilization
Changchun Institute of Applied Chemistry
Chinese Academy of Sciences, Changchun, 130022, (P. R. China)
E-mail: xbzhang@ciac.ac.cn
Homepage: http://energy.ciac.jl.cn

[b] F.-L. Meng,+ K.-H. Liu
Key Laboratory of Automobile Materials, Ministry of Education
Department of Materials Science and Engineering, Jilin University
Changchun 130012, Jilin (P. R. China)

[c] Q. Zhang+
Hunan Key Laboratory for Micro-Nano Energy Materials and Device
Department of Physics, Xiangtan University
Xiangtan, 411105, Hunan (P. R. China)

[+] *These authors contributed equally to this work.*

Supporting information and the ORCID identification number(s) for the author(s) of this article can be found under: https://doi.org/10.1002/chem.201903158.

Part of a Special Issue on Electrocatalysis: Mechanism and Applications. To view the complete issue, visit Issue 18, 2020.

performances, such as an enhanced partial current density and significantly improved faradaic efficiency of 94.1 % at an acceptable overpotential, which is attributed to the optimized exposed active sites, as confirmed by DFT calculations. Furthermore, a high energy conversion efficiency of 60.3 % and a satisfactory stability up to day–night are also reached.

The integrated 3D bismuth oxide ultrathin nanosheets/N-doped carbon foam electrode (devoted as BUNS/NCF) is facilely fabricated based on the sponge effect and N-atom anchor, which is schematically illustrated in Scheme 1. Initially, the N-doped carbon foam (NCF) is synthesized by direct two-step pyrolysis of melamine foam. The NCF is light weight and can maintain integrity without structural damage under different bending conditions, as well as high electrical conductivity (Figure S1 and S2, Supporting Information).

Then a strip of NCF is immersed into an autoclave for solvothermal growth of bismuth oxide ultrathin nanosheets. The SEM and TEM are first employed to explore the morphology and microstructure evolution (Figure 1 b–d). Obviously, a well-presented nanosheet array structure wraps the entire NCF surface homogeneously. The thickness of this 2D ultrathin nanostructure is confirmed to be 7.9 nm by the AFM image (Figure 1 f). XRD is then carried out to reveal the crystal structure evolution, wherein, after BUNS coating, all diffraction peaks of BUNS/NCF can be well indexed to the cubic phase of δ-Bi_2O_3 (PDF# 27-0052), the diffractions belonging to carbon decrease greatly (Figure 1 a). Figure 1 e displays the HR-TEM image of an as-prepared Bi_2O_3 nanosheet, the interplanar distance is measured to be 0.276 nm, corresponding to the d-spacing of (110) of Bi_2O_3. Energy dispersive X-ray spectroscopy (EDX) element mapping identifies the presence and uniform distribution of C, N, O, and Bi elements. XPS studies provide further evidence of

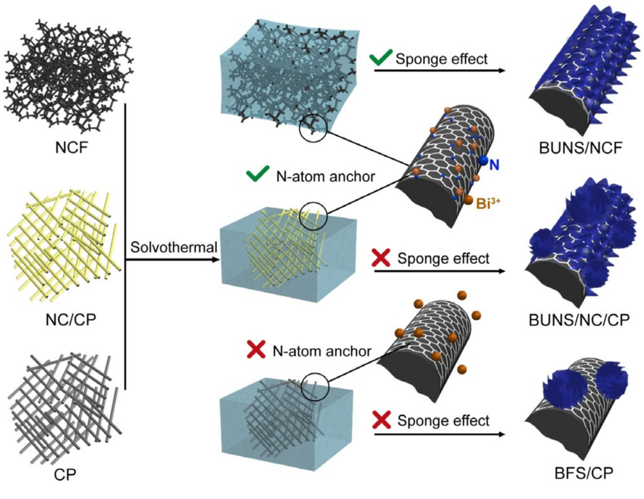

Scheme 1. Schematic diagram of the sponge effect and N-atom anchor in the preparation of uniform bismuth oxide foam electrodes of BUNS/NCF.

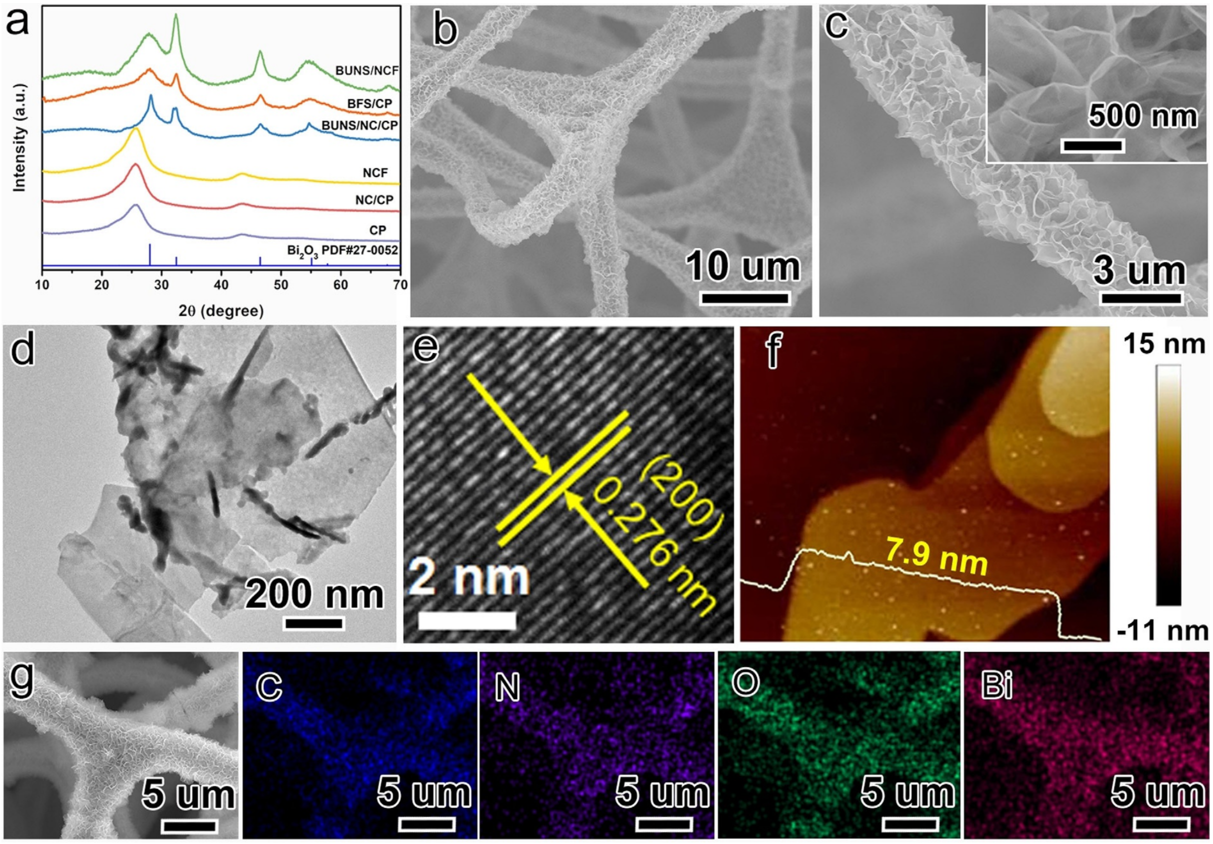

Figure 1. (a) XRD patterns of BUNS/NCF, BFS/CP, BUNS/NC/CP, NCF, NC/CP, and CP. (b, c) Low- and high-magnification SEM images of BUNS/NCF. (d) TEM image of BUNS/NCF. (e, f) HRTEM and AFM image of BUNS/NCF. (g) The selected area SEM image and corresponding EDS element mapping images of C, N, O, and Bi.

Bi_2O_3. Figure S3a, Supporting Information, presents the typical survey XPS spectrum of BUNS/NCF, in which, only Bi, C, O, and N elements can be observed. The binding energies of 159.1 and 164.4 eV in the high-resolution Bi 4f XPS spectra (Figure S3b, Supporting Information) reveal the Bi 4f 7/2 and Bi 4f 5/2 levels of Bi_2O_3, respectively. The N 1 s peaks at 400.2 and 398.5 eV are attributed to the graphitic-N, and pyridinic-N in NCF, respectively (Figure S3d, Supporting Information).

The N-doping and sponge effect of the 3D network carbonaceous foam substrate are expected to play a key role in forming the homogeneous nanosheet array structure, which are then discussed and tracked by the morphology variation on contrast substrates. Two different substrates including N-doped carbon shell/carbon paper (devoted as NC/CP) and pure carbon paper (CP) are put forward and compared. Figure S4, Supporting Information, reveals the uniform distribution of the polydopamine precursor shell and its derived N-doped carbon shell with rough surface and abundant defects. Both XRD and XPS studies reveal the presence of Bi_2O_3 on CP and NC/CP after solvothermal growth of Bi_2O_3 (Figure 1 a and Figure S5, Supporting Information). As shown in Figure S6, some irregular thick Bi_2O_3 sheets assembled into a large flower-like aggregated structure and are randomly anchored on CP (named as BFS/CP). Unlike that, many vertically oriented Bi_2O_3 nanosheets are interconnected with each other on NC/CP (devoted as BUNS/NC/CP) similar to BUNS/NCF (Figure S7, Supporting Information). Such contrast suggests the key role of the N-doped carbon layer, which should be able to form a coupling interaction between Bi ions and nitrogen species to effectively stabile the nucleation and assembly of Bi_2O_3 nanosheets onto NC/CP. In spite of this, compared to BUNS/NCF, lots of varisized Bi_2O_3 spheres composed of compact nanosheets are decorated on BUNS/NC/CP, indicating the secondary growths of Bi_2O_3 on Bi_2O_3 nanosheets. Besides, the Bi_2O_3 nanosheet on BUNS/NCF shows larger horizontal sizes. The sponge effect of carbon foam should promote the uniform growth of the Bi_2O_3 nanosheet, wherein, the fibrous skeleton draws in a current of reaction solution and provides enough space for growth.

The BUNS/NCF is then directly applied as the working electrode without extra substrates or binders for electrochemical CO_2 reduction experiments. Prior to that, the samples are activated electrochemically by subjecting a cathodic current of $-5.0\ mA\,cm^{-2}$ under CO_2 saturation until a stable potential is reached (Figure S8, Supporting Information). Constant potential electrolysis (Figure S9, Supporting Information) at a series of potentials are then performed with two hours to collect the liquid products, quantified by ^1H NMR spectroscopy. The gas products are determined by GC analysis, in which, only HCOOH, CO, and H_2 are detected (Figure S10, Supporting Information). Figure 2 a shows the total electrochemical reduction current density at different applied potentials. It is obvious that, both BUNS/NCF and BUNS/NC/CP display much higher current density than BFS/CP. A turning point in the current density, i.e. more negative than -0.9 V, appears between BUNS/NCF and BUNS/NC/CP, which should be caused by the relatively low conductivity of BUNS/NCF.

The Faradaic efficiency (FE) of HCOOH obtained for BUNS/NCF, BUNS/NC/CP, and BFS/CP as a function of potential are shown in Figure 2 b. Wherein, with the cathodic potentials are more negative than -0.7 V vs. RHE, and the FE of HCOOH increases rapidly for all three samples. Especially, the BUNS/NCF reaches a maximum FE of 94.1 % at a cathodic potential of -1.0 V, for BUNS/NC/CP and BFS/CP, that are 87.9 and 87.0 %,

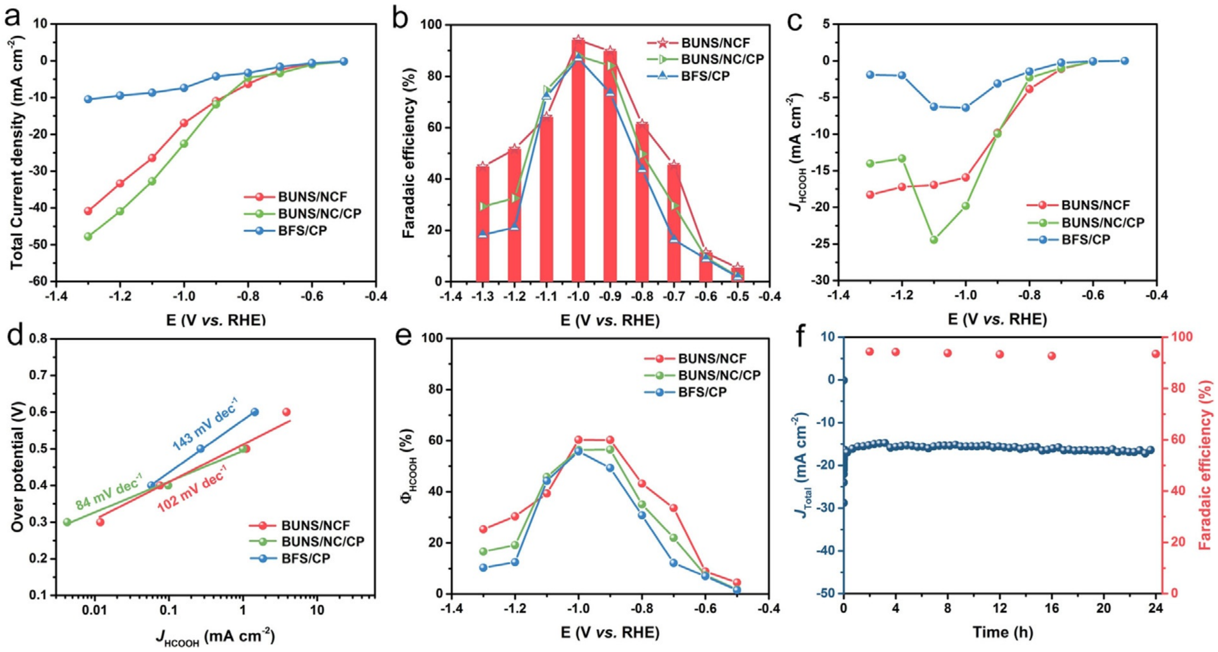

Figure 2. Electroreduction of CO_2 to HCOOH. Data are shown for BUNS/NCF, BUNS/NC/CP, and BFS/CP. (a) The total current density in CO_2-saturated 0.5 м $KHCO_3$ solution at different applied potentials. (b) The corresponding FE of HCOOH. (c) The partial current density for HCOOH at each given potential. (d) Tafel plots.

respectively. To the best of our knowledge, the high selectivity towards the HCOOH product of CO_2 convention exhibited by BUNS/NCF is among the highest reported result (Table S1, Supporting Information). Besides, in a wide potential range from -0.8 to -1.2 V, a high FE of HCOOH of more than 50% can be observed. In comparison, both BUNS/NC/CP and BFS/CP display higher FE values. Notably, the FE for CO formation remains at a very low level, under 9%, in the whole measured potential range, whether it be BUNS/NCF or BUNS/NC/CP, or BFS/CP (Figure S11, Supporting Information), meaning the superior single conversion or product selectivity of HCOOH for CO_2 reduction based on the Bi electrodes leaving out the competitive HER.

The partial current density of HCOOH formation (J_{HCOOH}) represents the incorporation of both the reaction rate and selectivity, which should be very comprehensive to reflect the practical activity of these electrodes. As shown in Figure 2c, the J_{HCOOH} of BUNS/NCF reaches the peak value of -18.3 mA cm^{-2} at -1.3 V. It's worth noting that, with the applied cathodic potentials of more negative than 0.9 V, the BUNS/NC/CP shows a higher J_{HCOOH} than BUNS/NCF until -1.1 V (reaching a peak value of -24.4 mA cm^{-2}), which should be attributed to better conductivity of BUNS/NC/CP derived from CP. But this trend stops after -1.1 V, indicating that a higher overpotential could not ensure a higher HCOOH yield; the heavily decreased FE may take major responsibility. The kinetic activities for CO_2 reduction of the three electrodes are then estimated by the corresponding Tafel plots (Figure 2d). The BUNS/NCF reveals a Tafel slope of approximately 102 mV/decade, which is slightly bigger than that of BUNS/NC/CP (84 mV/decade) and smaller than BFS/CP (143 mV/decade); similarly, the lower conductivity has limited its reaction rate. The Tafel slopes of the electrodes are near 118 mV/decade, which generally indicates the rate determining step (RDS) involves an initial one-electron transfer step from catalyst to CO_2.[9b] Electrochemical impedance spectroscopy (EIS) measurements are then conducted to provide a deep insight into the kinetics of the electron-transfer processes (Figure S12, Supporting Information), wherein, the BFS/CP displays smaller impedance arcs compared to the other samples, indicating lowest electron-transfer resistance. Despite low conductive NCF, the BUNS/NCF gives a narrow gap, which must be attributed to the remarkably uniform ultrathin 2D nanosheets without aggregation compared to BUNS/NC/CP and BFS/CP.

The significantly enhanced performance of the BUNS/NCF in comparison with that of BUNS/NC/CP and BFS/CP is partly due to its increased electrochemical surface area (ESCA), that could be alternatively reflected by the capacitive behavior. The capacitance of BUNS/NCF is measured to be 0.41 F cm^{-2}, higher than that of BUNS/NC/CP (0.35 F cm^{-2}) and BFS/CP (0.19 F cm^{-2}) (Figure S13, Supporting Information). The larger ECSA mainly stems from the consensual advantages of the advanced 3D nanosheet array foam electrode for a high utilization ratio of catalysts, including increased accessible surface area and accelerated mass transfer. But beyond that, the low-coordinated steps and edges in ultrathin 2D nanostructures should give rise to more exposed interior atoms in the process of surface reconstruction for enlarged exposure of active sites.

The characteristic cathodic energy converting efficiency (Φ_{HCOOH}) to the formation of HCOOH for above electrodes is evaluated according to the early reported papers.[10] Due to the low overpotential and high FE, the BUNS/NCF gives the highest energy efficiency of 60.3%, compared to BUNS/NC/CP (56.5%) and BFS/CP (55.7%) (Figure 2e), consequently distinguishing BUNS/NCF as a prospective electrode for produce of HCOOH based on the electrochemical CO_2 conversation system. One day and night continuous electrolysis test at an applied potential of -1.0 V with the highest FE is then carried out to evaluate the stability of BUNS/NCF. The products distribution against time is measured and the FE of HCOOH at intervals is calculated shown in Figure 2f. Obviously, almost negligible decay in current density could be observed, the FE keeps up essentially unchanged around 94% over 24 h, suggesting relatively stable performance in the time of the process.

The morphology, microstructure, and phase evolution after long-term electrolysis are then explored. XRD patterns confirm the exclusive metallic Bi (PDF#44-1246) after long-term electrolysis without any other phases except the peaks of carbonaceous substrates (Figure 3a). Further evidence of this evolution from Bi_2O_3 to Bi could be found by XPS studies (Figure 3b), the peaks at approximately 154.4 and 160.4 eV should be induced by the partial surface oxidation when exposed in air. As SEM and TEM images shown in Figure 3c–f, the 3D nanosheet array structure reserves to a certain degree, except for the difference that discontinuous and much rough nanosheets composed of abundant nanoparticles replace the smooth ones, as well as containing numerous pores and grain boundaries. These decided changes should be induced by the reduction reaction of Bi_2O_3 and surface reorganization in the catalytic process. An interplanar distance of 0.227 nm appears in the HRTEM image (Figure 3f inset), which corresponds to resolved lattice fringes of Bi (110) plane. The BUNS/NC/CP exhibits a similar situation, but with more serious array structure damage (Figure S14, Supporting Information), and the lattice fringe of Bi (012) plane with a spacing of 0.328 nm is observed in the HRTEM image. For BFS/CP, the large flowerlike aggregated structure turns into porous hierarchical structure (Figure S15, Supporting Information). These above results indeed indicate that the active catalyst under catalytic turnover condition is Bi as early reported.[9b,c]

Though the polycrystalline Bi exhibits excellent electrocatalytic performances and high selectivity for the reduction of CO_2 into HCOOH. The underlying reaction mechanism is still uncertain. Besides, the reduction of the CO_2 into HCOOH is always accompanied by some compete reaction, such as the reduction of CO_2 into CO and the hydrogen evolution reaction, which are important to understand the reaction mechanism and design the highly efficient function-oriented catalyst. Therefore, the first principle calculations based on DFT were conducted to lift the veils. As shown in Figure 4a, in contrast with the Bi (104) and Bi (012), Bi (110) exhibits slightly higher activity towards the reduction of CO_2 into HCOOH due to the smaller ΔG_{RDS}. The value of the ΔG_{RDS} of CO_2 reduction into

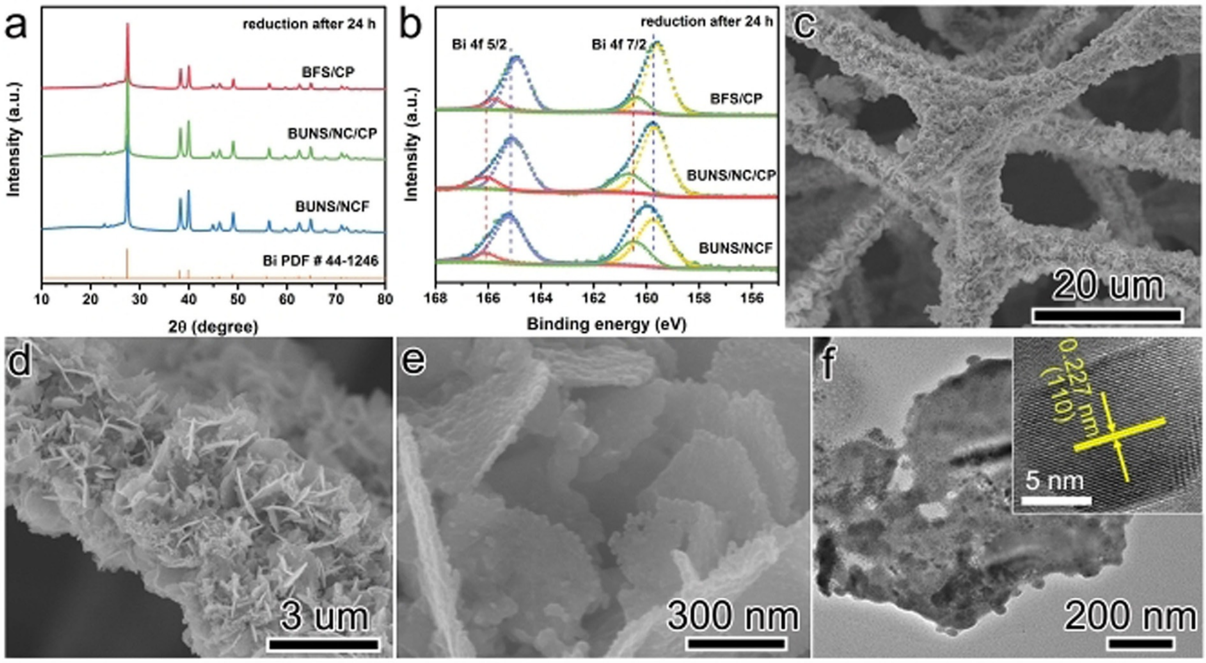

Figure 3. Morphology, structural, and component characterization after long-term electrolysis. (a) XRD patterns and (b) Bi 4f XPS spectra of BUNS/NCF, BUNS/NC/CP, and BFS/CP after 24 h continuous reduction. (c–e) Low- and high-magnification SEM images of BUNS/NCF after 24 h continuous reduction. (f) The corresponding TEM image (inset: HRTEM image).

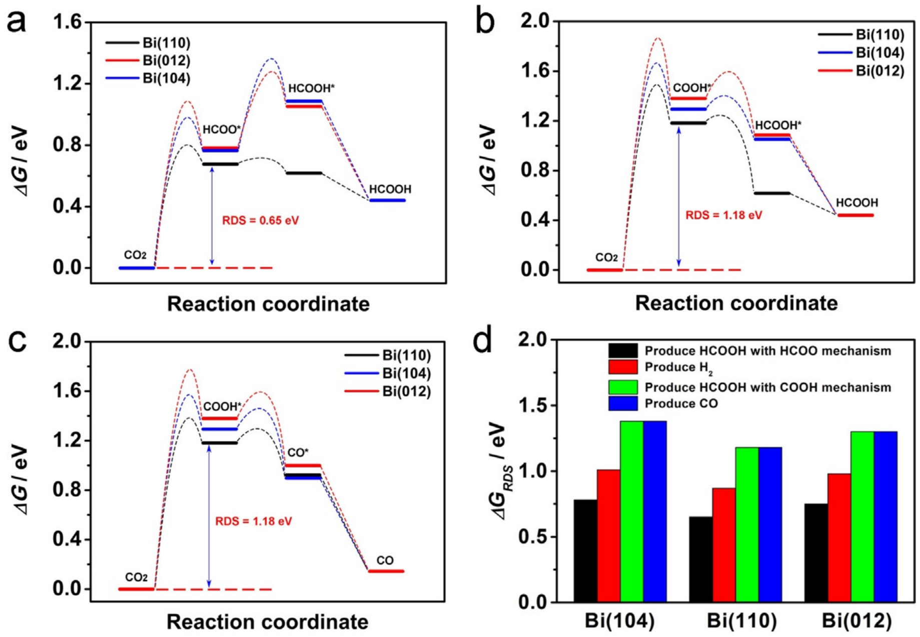

Figure 4. (a) Gibbs free energy diagrams of the polycrystalline Bi toward the reduction of CO_2 into HCOOH with HCOO mechanism. (b) Gibbs free energy diagrams of the polycrystalline Bi toward the reduction of CO_2 into HCOOH with COOH mechanism. (c) Gibbs free energy diagrams of the polycrystalline Bi toward the reduction of CO_2 into CO. (d) Gibbs free energy of the rate-determining step for the polycrystalline Bi toward various reduction reactions.

HCOOH with the HCOO mechanism on Bi(110) is 0.65 eV, which is smaller than that of this reaction with the COOH mechanism (Figure 4) and these compete reactions (the reduction of CO_2 into CO and HER) shown in Figure 4c and d, indicate the reduction of CO_2 into HCOOH tends to proceed with the HCOO mechanism at lower theoretical overpotential with high selectivity on Bi(110), which is in agreement with the experimental observations. Meanwhile, accelerated electron transfer and mass diffusion induced by the 3D NCF electrode provide a synergistic effect along with the exposed high selectivity active sites.

In summary, we have designed and fabricated an integrated BUNS/NCF electrode composed of an ultrathin nanosheets array structure wrapping 3D carbon foam framework with flexibility. Benefiting from the large special surface area, exposure and accessibility of active sites, and high efficiency mass transfer, the developed integrated BUNS/NCF electrode shows significantly enhanced electrocatalytic performance for selective convention from CO_2 to HCOOH with an enhanced partial current density and significantly improved FE as high as 94.1% at a moderate overpotential. Additionally, the active integrated foam electrode realizes the conversion of CO_2 to HCOOH under a high energy conversion efficiency of 60.3% and with long-term durability. The developed synthetic approach pioneers new methods towards the development of sustainable 3D array structured foam electrodes with excellent performance for other key electrochemical energy conversion and storage technologies.

Acknowledgements

This work was financially supported by the Ministry of Science and Technology of the People's Republic of China (Grant No. 2016YFB0100103), the National Program on Key Basic Research Project of China (2014CB932300), and the National Natural Science Foundation of China (21422108 and 51472232).

Conflict of interest

The authors declare no conflict of interest.

Keywords: bismuth oxide · CO_2 reduction · electrocatalysis · formic acid · integrated foam electrode

[1] a) M. Asadi, B. Kumar, A. Behranginia, B. A. Rosen, A. Baskin, N. Repnin, R. F. Klie, *Nat. Commun.* **2014**, *5*, 4470; b) C. Costentin, M. Robert, J. M. Savéant, *Chem. Soc. Rev.* **2013**, *42*, 2423.

[2] a) Q. Lu, J. Rosen, Y. Zhou, G. S. Hutchings, Y. C. Kimmel, J. G. Chen, F. Jiao, *Nat. Commun.* **2014**, *5*, 3242; b) M. Ma, K. Djanashvili, W. A. Smith, *Angew. Chem. Int. Ed.* **2016**, *55*, 6680; *Angew. Chem.* **2016**, *128*, 6792.

[3] a) W. H. Wang, Y. Himeda, J. T. Muckerman, G. F. Manbeck, E. Fujita, *Chem. Rev.* **2015**, *115*, 12936; b) Z. Weng, J. Jiang, Y. Wu, Z. Wu, X. Guo, K. L. Materna, H. Wang, *J. Am. Chem. Soc.* **2016**, *138*, 8076.

[4] a) R. Kortlever, I. Peters, S. Koper, M. T. Koper, *ACS Catal.* **2015**, *5*, 3916; b) K. Manthiram, B. J. Beberwyck, A. P. Alivisatos, *J. Am. Chem. Soc.* **2014**, *136*, 13319.

[5] a) J. Wu, R. M. Yadav, M. Liu, P. P. Sharma, C. S. Tiwary, L. Ma, P. M. Ajayan, *ACS Nano* **2015**, *9*, 5364; b) S. Lin, C. S. Diercks, Y. B. Zhang, N. Kornienko, E. M. Nichols, Y. Zhao, C. J. Chang, *Science* **2015**, *349*, 1208; c) M. Asadi, K. Kim, C. Liu, A. V. Addepalli, P. Abbasi, P. Yasaei, P. Zapol, *Science* **2016**, *353*, 467.

[6] a) D. Gao, H. Zhou, J. Wang, S. Miao, F. Yang, G. Wang, X. Bao, *J. Am. Chem. Soc.* **2015**, *137*, 4288; b) P. P. Sharma, J. Wu, R. M. Yadav, M. Liu, C. J. Wright, C. S. Tiwary, X. D. Zhou, *Angew. Chem. Int. Ed.* **2015**, *54*, 13701; *Angew. Chem.* **2015**, *127*, 13905.

[7] a) D. Ren, Y. Deng, A. D. Handoko, C. S. Chen, S. Malkhandi, B. S. Yeo, *ACS Catal.* **2015**, *5*, 2814; b) Y. Chen, C. W. Li, M. W. Kanan, *J. Am. Chem. Soc.* **2012**, *134*, 19969.

[8] K. S. Kim, W. J. Kim, H. K. Lim, E. K. Lee, H. Kim, *ACS Catal.* **2016**, *6*, 4443.

[9] a) J. Medina-Ramos, J. L. DiMeglio, J. Rosenthal, *J. Am. Chem. Soc.* **2014**, *136*, 8361; b) H. Zhong, Y. Qiu, T. Zhang, X. Li, H. Zhang, X. Chen, *J. Mater. Chem. A* **2016**, *4*, 13746; c) W. Lv, J. Zhou, J. Bei, R. Zhang, L. Wang, Q. Xu, W. Wang, *Appl. Surf. Sci.* **2017**, *393*, 191; d) J. Qiao, Y. Liu, F. Hong, J. Zhang, *Chem. Soc. Rev.* **2014**, *43*, 631.

[10] a) D. Preti, S. Squarcialupi, G. Fachinetti, *Angew. Chem. Int. Ed.* **2010**, *49*, 2581; *Angew. Chem.* **2010**, *122*, 2635; b) C. C. Tai, T. Chang, B. Roller, P. G. Jessop, *Inorg. Chem.* **2003**, *42*, 7340.

[11] T. Schaub, R. A. Paciello, *Angew. Chem. Int. Ed.* **2011**, *50*, 7278; *Angew. Chem.* **2011**, *123*, 7416.

[12] S. Berardi, S. Drouet, L. Francàs, C. G. Suriñach, M. Guttentag, C. Richmond, A. Llobet, *Chem. Soc. Rev.* **2014**, *43*, 7501.

[13] a) F. Li, L. Chen, G. P. Knowles, D. R. MacFarlane, J. Zhang, *Angew. Chem. Int. Ed.* **2017**, *56*, 505; *Angew. Chem.* **2017**, *129*, 520; b) D. Raciti, K. J. Livi, C. Wang, *Nano Lett.* **2015**, *15*, 6829.

[14] a) X. Lu, C. Zhao, *Nat. Commun.* **2015**, *6*, 6616; b) J. Wang, H. X. Zhong, Y. L. Qin, X. B. Zhang, *Angew. Chem. Int. Ed.* **2013**, *52*, 5248; *Angew. Chem.* **2013**, *125*, 5356.

Manuscript received: July 10, 2019
Revised manuscript received: August 27, 2019
Accepted manuscript online: September 3, 2019
Version of record online: October 15, 2019